Method for spatially resolved imaging of energy-dependent photoelectron diffraction

S. Y. Tong and H. Huang
Laboratory for Surface Studies and Department of Physics, University of Wisconsin-Milwaukee, Milwaukee, Wisconsin 53201

C. M. Wei
Institute of Physics, Academia Sinica, Nankang, Taipei, Taiwan 11529, Republic of China
(Received 27 November 1991; revised manuscript received 3 March 1992)

We present a method for spatially resolved imaging of energy-dependent photoelectron diffraction. Energy-dependent photoelectron-diffraction spectra are individually Fourier transformed to three-dimensional vector space. The complex transformed amplitudes are summed over a span of ϕ angles or over a span of polar angles. The images are, respectively, well resolved in the radial and azimuthal directions, or in the radial and polar directions. The intersections of these real-space maps fix the atomic coordinates. We show how the intensity loci from single and multiple scattering paths are separately resolved and how most multiple scattering contributions are eliminated. By varying the collection angles, atoms in different regions relative to the emitter, e.g., surface or bulk atoms, are imaged. One can also use the photon's **A** vector to enhance the near-π backscattering geometry. We compare this method with another direct method: extended x-ray-absorption fine structure.

I. INTRODUCTION

It has always been a major goal in structural analysis to develop direct methods which invert diffraction data to reveal the atomic arrangement. In photoelectron diffraction, such a direct method was carried out by Hussain *et al.* in 1981 (Ref. 1) who Fourier integrated energy-dependent photoelectron-diffraction (EDPD) spectra. The variable in the Fourier integral was a scalar quantity ξ which Orders and Fadley[2] pointed out to correspond to the single-scattering path difference between the direct (reference) wave and the scattered (object) wave. This method works in a manner analogous to extended x-ray-absorption fine structure (EXAFS) in that the Fourier transformed peaks are analyzed to yield scalar distances between an emitting atom and its neighboring atoms. Barton, Shirley, and co-workers[3-5] used this analogy to call this approach angle-resolved photoemission extended fine structure (ARPEFS). The particular method does not yield directly individual atomic positions; rather, all scatterers having the same path-length difference ξ contribute to the same peak in the Fourier transform.

In this paper, we introduce the concept of spatially resolved imaging of energy-dependent photoelectron diffraction (SRI-EDPD) spectra. In SRI-EDPD, we express the scalar function ξ in terms of the vector atomic position **R** in the Fourier integral of EDPD spectra. We then sum these Fourier integrals over a span of ϕ angles or over a span of polar angles. The images we obtain are respectively well resolved in the radial and azimuthal directions or in the radial and polar directions. The intersections of these real-space maps fix the atomic coordinates.

The approach of SRI-EDPD is a variation of the summed-energy electron-emission holography (EEH) introduced earlier (Refs. 6 and 7) The method is based on a microscopic description of the photoelectron-diffraction process, and it provides a clear connection between multiple-energy EEH (Refs. 6 and 7) and the earlier method of ARPEFS.[1-5] In addition, SRI-EDPD offers a number of special features: For example, one can use the photon's **A** vector to enhance the near-π back-scattering geometry similar to ARPEFS.[3] With **A** and the electron's exit direction $\hat{\mathbf{k}}$ pointing in nearly the same directions, the images of atoms lying directly *behind* the emitter are particularly bright. By choosing EDPD spectra at near glancing directions, bulk-emission contributions can be minimized. This geometry is critical for imaging surface reconstruction of clean materials, e.g., GaAs(100)-2×4, etc., as we shall present elsewhere. Also, this approach provides a pictorial view that explains how most multiple scattering contributions are eliminated. SRI-EDPD can be viewed as an extension of the small-window energy-extension process (SWEEP) introduced earlier.[7-9] However, this approach requires considerably less data base than earlier multiple-energy EEH methods. By using intersections of real-space images, which are well-resolved in the radial and azimuthal *or* polar directions, the data base used scales linearly as $(N_\theta+N_\phi)$, instead of the quadratic dependence $(N_\theta\times N_\phi)$. Here, N_θ or N_ϕ is the number of mesh points used in the polar or azimuthal direction, respectively. In the following sections, we shall present details of these features together with illustrative examples. We shall also discuss the relationship between this method and another direct technique: EXAFS.

II. METHOD OF SRI-EDPD

In the Fourier transformation of Hussain *et al.*[1] of EDPD data, the integral extracts a scalar length ξ as

$$\phi_{\hat{\mathbf{k}}}(\xi)=\int_{k_{\min}}^{k_{\max}}\chi(k\hat{\mathbf{k}})e^{-ik\xi}g(\mathbf{k})dk\ , \tag{1}$$

where $\chi(k\hat{\mathbf{k}})=I(k\hat{\mathbf{k}})/I_D(k\hat{\mathbf{k}})-A$ is the normalized EDPD spectra in direction $\hat{\mathbf{k}}$ and $g(k)$ is a window function which ensures that $\chi(k\hat{\mathbf{k}})$ begins and ends at nodal points.[1] $I_D(k\hat{\mathbf{k}})$ is the atomic (reference) emission intensity and A is the *energy* average of $I(k\hat{\mathbf{k}})/I_D(k\hat{\mathbf{k}})$. With experimentally measured $I(k\hat{\mathbf{k}})$, one can use an N-point-moving average for $I_D(k\hat{\mathbf{k}})$ and set $A=1$. In SRI-EDPD, we replace the single-scattering path difference ξ by $\{R-\hat{\mathbf{k}}\cdot\mathbf{R}\}$ and write the transform in terms of the vector $\mathbf{R}$,

$$\phi_{\hat{\mathbf{k}}}(\mathbf{R})=\int_{k_{\min}}^{k_{\max}}\chi(k\hat{\mathbf{k}})e^{-ikR}e^{i\mathbf{k}\cdot\mathbf{R}}g(k)dk\ . \tag{2}$$

In $\chi(k\hat{\mathbf{k}})$, for an atom at $\mathbf{R}_1$ (relative to the emitting atom) its single-scattering contribution is[8-10]

$$\chi(k\hat{\mathbf{k}})\sim\cdots+F_D(\hat{\mathbf{R}}_1)F_D^{-1}(\hat{\mathbf{k}})f(\hat{\mathbf{k}}\cdot\hat{\mathbf{R}}_1)\times\frac{e^{ikR_1}e^{-i\mathbf{k}\cdot\mathbf{R}_1}}{R_1}+\cdots\ , \tag{3}$$

where $F_D(\hat{\mathbf{R}}_1)$ and $F_D^{-1}(\hat{\mathbf{k}})$ are factors related to the photoexcitation matrix elements[11] and $f(\hat{\mathbf{k}}\cdot\hat{\mathbf{R}}_1)$ is the atomic scattering factor. The phase shifts due to these factors could displace atomic positions by $\sim\pm0.3$ Å.[9] Disregarding such shifts for the moment, if we substitute Eq. (3) into Eq. (2), the function $|\phi_{\hat{\mathbf{k}}}(\mathbf{R})|$ is a maximum along the locus

$$\xi=R-\hat{\mathbf{k}}\cdot\mathbf{R}=R_1-\hat{\mathbf{k}}\cdot\mathbf{R}_1\ . \tag{4}$$

However, if there are other atoms $\mathbf{R}_2,\mathbf{R}_3,\ldots$ in the solid with the same single-scattering path difference,[2] i.e., if

$$R_i-\hat{\mathbf{k}}\cdot\mathbf{R}_i=R_1-\hat{\mathbf{k}}\cdot\mathbf{R}_1\ , \tag{5}$$

then the positions of these other atoms must fall on the same locus. The situation is depicted schematically in Fig. 1, where $\mathbf{R}_1$ and $\mathbf{R}_2$ have the same single-scattering path difference with respect to an EDPD spectrum in direction $\hat{\mathbf{k}}$.

This ambiguity, however, is lifted for $\mathbf{R}_1$ and $\mathbf{R}_2$ if we consider another EDPD spectrum in a different direction, e.g., $\hat{\mathbf{k}}'$. The new loci, $C_{\hat{\mathbf{k}}',1}$ and $C_{\hat{\mathbf{k}}',2}$ are spatially resolved. Mathematically, this reflects the fact that if

$$R_1-\hat{\mathbf{k}}\cdot\mathbf{R}_1=R_2-\hat{\mathbf{k}}\cdot\mathbf{R}_2\ , \tag{5a}$$

then

$$R_1-\hat{\mathbf{k}}'\cdot\mathbf{R}_1\neq R_2-\hat{\mathbf{k}}'\cdot\mathbf{R}_2 \tag{5b}$$

for any two atoms $\mathbf{R}_1\neq\mathbf{R}_2$ and two directions $\hat{\mathbf{k}}\neq\hat{\mathbf{k}}'$. By using five to ten EDPD spectra along different exit directions, the loci intersect to form bright "spots" when viewed along specific cut planes. These spots provide spatially resolved information of atomic positions $\mathbf{R}_1,\mathbf{R}_2,\ldots,\mathbf{R}_N$ in these planes of view.

Mathematically, we obtain the spatially resolved information by summing the complex Fourier functions over a span of exit directions

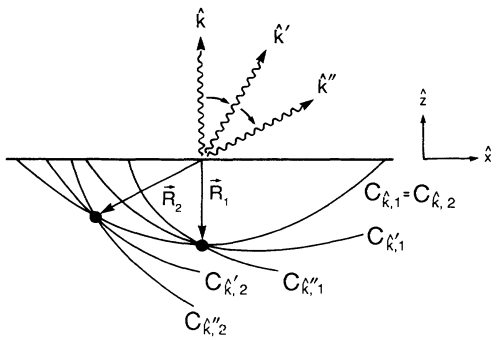

FIG. 1. Intensity loci due to single-scattering path differences for atoms $\mathbf{R}_1$, $\mathbf{R}_2$ and emission directions $\hat{\mathbf{k}}$, $\hat{\mathbf{k}}'$, and $\hat{\mathbf{k}}''$. The $\hat{\mathbf{z}}$ axis points from surface to vacuum. The intersections of the contours (dots) produce spatially resolved images in the xz plane.

$$\phi(\mathbf{R})=\sum_{j=1}^{N}\phi_{\hat{\mathbf{k}}_j}(\mathbf{R})\ . \tag{6}$$

The atomic images are obtained by one of the following absolute functions:

$$u_1(\mathbf{R})=|\phi(\mathbf{R})| \tag{7a}$$

or

$$u_2(\mathbf{R})=|\phi(\mathbf{R})|^2 \tag{7b}$$

or

$$u_3(\mathbf{R})=|R\phi(\mathbf{R})|^2\ , \tag{7c}$$

in particular, $u_3(\mathbf{R})$ compensates for the radial falloff of the reference wave.

In the above discussion, only single-scattering path lengths are considered. Multiple scattering creates additional path differences and their effect must be considered. In the next section, we will explain how most multiple scattering effects are eliminated in the SRI-EDPD process.

III. EFFECTS OF MULTIPLE SCATTERING

A photoelectron generally undergoes a number of multiple scatterings before leaving a solid. The path-length difference $\xi=R-\hat{\mathbf{k}}\cdot\mathbf{R}$ that was pointed out by Orders and Fadley,[2] applied only to the single-scattering case. For an atom at $\mathbf{R}_\beta$, multiple scattering creates new path differences, and now we consider their effects.

If we place the origin of the coordinate system at atom α, which is the emitter, the photoelectron wave function is given by[11,12]

$$\psi(\mathbf{r})=\phi_D(\mathbf{r})+\psi_s(\mathbf{r})\ , \tag{8}$$

where

$$\psi_D(\mathbf{r})=ik\sum_L h_l^{(1)}(kr)Y_L(\hat{\mathbf{r}})m_L^{\alpha} \tag{9a}$$

$$=\frac{e^{ikr}}{r}F_D(\hat{\mathbf{k}}),\quad r\to\infty \tag{9b}$$

is the reference wave. In obtaining Eq. (9b), we have set $A_L^\alpha = ikm_L^\alpha$, which contains the photoexcitation matrix elements,[10,13] and

$$F_D(\hat{\mathbf{k}}) = \frac{1}{k}\sum_L i^{-(l+1)} Y_L(\hat{\mathbf{r}}) A_L^\alpha \tag{10}$$

is the amplitude of the unscattered wave.[10] There are many scattering paths in multiple scattering, and for this discussion, it is best to group these paths according to the *last scattering event*. Thus, for an atom at $\mathbf{R}_\beta$, the scattered wave that leaves the solid after the last scattering from this atom is[10-13]

$$\psi_s(\mathbf{r}) = \sum_L h_l^{(1)}(k|\mathbf{r}-\mathbf{R}_\beta|) Y_L(\widehat{\mathbf{r}-\mathbf{R}_\beta}) \left[\sum_{L''} t_l^\beta G_{LL''}^{\beta\alpha}(\mathbf{R}_\beta) A_{L''}^\alpha + \sum_{L'L''} t_l^\beta G_{LL'}^{\beta\gamma}(\mathbf{R}_\beta - \mathbf{R}_\gamma) t_{l'}^\gamma G_{L'L''}^{\gamma\alpha}(\mathbf{R}_\gamma) A_{L''}^\alpha + \cdots \right] + \cdots . \tag{11}$$

The first term in Eq. (11) is the single-scattering event at $\mathbf{R}_\beta$, the second term includes an intermediate scattering at atom $\mathbf{R}_\gamma$ before scattering at $\mathbf{R}_\beta$, and so on. In Eq. (11), the t matrix and structural propagators are given by[10]

$$t_l^\alpha = \frac{e^{2i\delta_l^\alpha} - 1}{2} \tag{12}$$

and

$$G_{L'L}(\mathbf{R}) = 4\pi \sum_{L''} i^{l'-l+l''} h_{l''}(kR) Y_{L''}(\hat{\mathbf{R}}) \times \int Y_{L'}^*(\Omega) Y_L(\Omega) Y_{L''}^*(\Omega) d\Omega , \tag{13}$$

respectively.[10] Following Ref. 10, we use the small-atom approximation form for $G_{L'L}(\mathbf{R})$, i.e.,

$$G_{L'L}(\mathbf{R}) = -4\pi i i^{l'-l} \frac{e^{ikR}}{kR} Y_{L'}^*(\hat{\mathbf{R}}) Y_L(\hat{\mathbf{R}}) \tag{14}$$

and the plane-wave scattering factor is[8,10]

$$f(\hat{\mathbf{k}}\cdot\hat{\mathbf{R}}) = \frac{4\pi}{ik}\sum_L Y_L(\hat{\mathbf{k}}) t_l Y_L^*(\hat{\mathbf{R}}) . \tag{15}$$

Then we can write $\psi_s(\mathbf{r})$ in Eq. (11) as

$$\psi_s(\mathbf{r}) = \frac{e^{ikr}}{r}\left[f(\hat{\mathbf{k}}\cdot\hat{\mathbf{R}}_\beta) F_D(\hat{\mathbf{R}}_\beta) \frac{e^{ikR_\beta}}{R_\beta} + f(\hat{\mathbf{k}}\cdot\widehat{R_\beta - R_\gamma}) f(\widehat{R_\beta - R_\gamma}\cdot\hat{\mathbf{R}}_\gamma) F_D(\hat{\mathbf{R}}_\gamma) \frac{e^{ikR_\gamma}}{R_\gamma}\frac{e^{ik|\mathbf{R}_\beta-\mathbf{R}_\gamma|}}{|\mathbf{R}_\beta-\mathbf{R}_\gamma|} + \cdots \right] e^{-i\mathbf{k}\cdot\mathbf{R}_\beta} + \cdots , \quad r\to\infty . \tag{16}$$

It is possible to correct for curved-wave effects in Eq. (16) by including in $f(\hat{\mathbf{k}}\cdot\hat{\mathbf{R}})$ the necessary correction terms as demonstrated by Rehr and Albers.[14] Using Eq. (16), we can write down explicitly the different orders of scattering contributions to $\chi(k\hat{\mathbf{k}})$ for paths that last scatter from atom $\mathbf{R}_\beta$,

$$\chi(k\hat{\mathbf{k}}) \sim \cdots + \left[f(\hat{\mathbf{k}}\cdot\hat{\mathbf{R}}_\beta) F_D(\hat{\mathbf{R}}_\beta) F_D^{-1}(\hat{\mathbf{k}}) \frac{e^{ikR_\beta}}{R_\beta} + f(\hat{\mathbf{k}}\cdot\widehat{R_\beta - R_\gamma}) f(\widehat{R_\beta - R_\gamma}\cdot\hat{\mathbf{R}}_\gamma) F_D(\hat{\mathbf{R}}_\gamma) F_D^{-1}(\hat{\mathbf{k}}) \frac{e^{ikR_\gamma}}{R_\gamma}\frac{e^{ik|\mathbf{R}_\beta-\mathbf{R}_\gamma|}}{|\mathbf{R}_\beta-\mathbf{R}_\gamma|} + \cdots \right] e^{-i\mathbf{k}\cdot\mathbf{R}_\beta} + \cdots \tag{17}$$

$$= \cdots + \left[A(\mathbf{k}) \frac{e^{ikR_\beta}}{R_\beta} + B(\mathbf{k}) \frac{e^{ikR_\gamma}}{R_\gamma}\frac{e^{ik|\mathbf{R}_\beta-\mathbf{R}_\gamma|}}{|\mathbf{R}_\beta-\mathbf{R}_\gamma|} + \cdots \right] e^{-i\mathbf{k}\cdot\mathbf{R}_\beta} + \cdots . \tag{18}$$

Again, the factors

$$A(\mathbf{k}) = f(\hat{\mathbf{k}}\cdot\hat{\mathbf{R}}_\beta) F_D(\hat{\mathbf{R}}_\beta) F_D^{-1}(\hat{\mathbf{k}})$$

and

$$B(\mathbf{k}) = f(\hat{\mathbf{k}}\cdot\widehat{\mathbf{R}_\beta - \mathbf{R}_\gamma}) f(\widehat{R_\beta - R_\gamma}\cdot\hat{\mathbf{R}}_\gamma) F_D(\hat{\mathbf{R}}_\gamma) F_D^{-1}(\hat{\mathbf{k}})$$

contribute to phase shifting the image position. Ignoring these phase-shift effects for the moment, we see that the first (explicit) term in Eq. (18) corresponds to the single-scattering path difference $\xi = R_\beta - \hat{\mathbf{k}}\cdot\mathbf{R}_\beta$. Multiple scattering generates additional path-differences given by, e.g., $\eta = \rho_\beta - \hat{\mathbf{k}}\cdot\mathbf{R}_\beta$, where $\rho_\beta = R_\gamma + |\mathbf{R}_\beta - \mathbf{R}_\gamma|$, and so on. Substituting $\chi(k\hat{\mathbf{k}})$ into Eq. (2) generates intensity maxima having loci satisfying the relation

$$\eta = R - \hat{\mathbf{k}}\cdot\mathbf{R} = \rho_\beta - \hat{\mathbf{k}}\cdot\mathbf{R}_\beta . \tag{19}$$

Therefore, in general, an atom at $\mathbf{R}_\beta$ generates a set of high-intensity loci ξ, η, etc., corresponding to single as well as higher orders of scattering. It also means that the scalar integral used in ARPEFS produces intensity peaks corresponding to single as well as higher orders of

scattering. The difficulty is that the high-intensity loci due to multiple scattering paths are not simply related to the atomic position $\mathbf{R}_\beta$.

To obtain specific atomic position information, we again make use of EDPD spectra along different $\hat{\mathbf{k}}$ directions. The solution of Eq. (19), i.e.,

$$R=\frac{\rho_\beta-\hat{\mathbf{k}}\cdot\mathbf{R}_\beta}{1-\hat{\mathbf{k}}\cdot\hat{\mathbf{R}}} \tag{20}$$

is *independent* of $\hat{\mathbf{k}}$ if and only if

$$\rho_\beta=R_\beta \tag{21a}$$

and

$$\hat{\mathbf{R}}\|\hat{\mathbf{R}}_\beta\ . \tag{21b}$$

With these two conditions satisfied, the solution of Eq. (20) is $R=R_\beta$, and together with condition Eq. (21b) yields $\mathbf{R}=\mathbf{R}_\beta$. In other words, only at $\mathbf{R}=\mathbf{R}_\beta$ would all the loci for different $\hat{\mathbf{k}}$ directions intersect at a single point. Therefore, while multiple scattering paths generate a multitude of high-intensity loci, these loci do not all intersect at a single point. As a result, the intensity in real space due to multiple scattering paths is weak compared to the intensity at true atomic positions $\mathbf{R}=\mathbf{R}_\beta$. Figure 2 depicts the single-scattering and multiple scattering loci for different directions arising from an atom at $\mathbf{R}_1$. In this example, the multiple scattering path ρ_1 is set equal to $2R_1$.

There are, however, "mixed" multiple scattering terms in $\chi(k\hat{\mathbf{k}})$, which are not eliminated by the integral in Eq. (2). These "mixed" multiple scattering events affect particularly strongly systems in which atoms line up in the forward or near-forward scattering directions. The effects of these "mixed" multiple scattering terms are presented elsewhere.[15]

While the intersections in Figs. 1 and 2 are well resolved in the x-z plane, they are poorly resolved in the direction along the y axis, because $\hat{\mathbf{k}}$, $\hat{\mathbf{k}}'$, etc., all lie in the x-z plane. To fix the *vector* coordinates of an atom, we sum in Eq. (6) EDPD spectra over two intersecting planes. If we adopt a convention in which the lower-case letter (δ) indicates good resolution and the capital letter (D) indicates poor resolution, the intersections of images with resolution characterized by $\delta R\,\delta\theta D\phi$ and $\delta R D\theta\delta\phi$ fix the positions of atoms in real space (see the second example given in Sec. IV and also Fig. 4). To determine the all-important emitter-to-scatterer (i.e., radial) resolution ΔR, we deduce from Eq. (1) that $\Delta\xi=1.2\Gamma$,[7,8,16] where $\Gamma=2\pi/(k_{\max}-k_{\min})$. Since $\Delta\xi=\Delta R(1-\cos\theta_s)$, where θ_s is the angle between $\hat{\mathbf{k}}$ and $\hat{\mathbf{R}}$; in the back-scattering geometry, $\theta_s\approx\pi$, and we obtain

$$\Delta R=\frac{2.4\pi}{(1-\cos\theta_s)(k_{\max}-k_{\min})} \tag{22}$$

$$\approx\frac{1.2\pi}{(k_{\max}-k_{\min})}\ . \tag{23}$$

On the other hand, the diffraction limit from the Helmholtz-Kirchhoff integral[17] at the maximum energy is $\Gamma(k_{\max})=2.4\pi/k_{\max}$.[8,16] This means if $k_{\max}>2k_{\min}$,

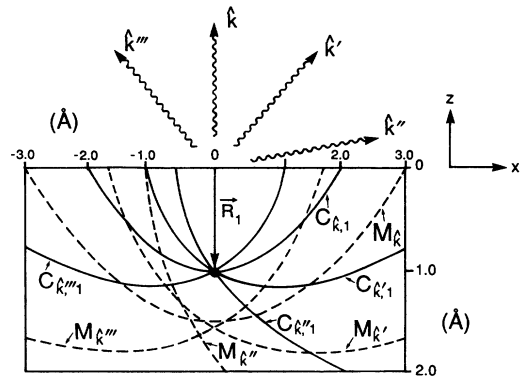

FIG. 2. Single-scattering contours (solid lines) and multiple scattering contours (broken lines) corresponding to an atom at $\mathbf{R}_1$ and emission directions $\hat{\mathbf{k}}$, $\hat{\mathbf{k}}'$, $\hat{\mathbf{k}}''$, $\hat{\mathbf{k}}'''$. A multiple scattering path length of $\rho_1=2$ Å is used.

the expression of Eq. (23) indicates that in the back-scattering geometry, the radial resolution from multiple energies is better than that of the single maximum energy.[16]

The situation is completely different in the forward-scattering geometry because there, $\theta_s\approx 0°$, and the resolution ΔR given by Eq. (22) is extremely poor. For example, using a typical scattering angle of $\theta_s=30°$ and $k_{\max}=2k_{\min}$, we obtain a ratio $\Delta R/\Gamma(k_{\max})\simeq 15$, i.e., in the forward-scattering geometry, the wave number integral in Eq. (2) produces images whose radial resolution is much poorer than those of the single maximum energy. In the second example Sec. IV (e.g., Fig. 5), we shall show images reconstructed from back-scattering and forward-scattering diffraction fringes and compare their respective resolutions. This is also why a different phase factor than that used in Eq. (2) is needed to sum holograms at multiple energies in the forward-scattering geometry in the conventional use of SWEEP.[7,8]

IV. APPLICATIONS OF SRI-EDPD: Cu(111) (1×1)-Co AND Ni(001)c(2×2)-S

In the first example, we demonstrate the use of SRI-EDPD in imaging neighboring atoms in the *same* layer as the emitter. We consider one monolayer (1 ML) of Co atoms occupying bulk-continuation sites on Cu(111). The Co layer is assumed to be pseudomorphic with the Cu(111) substrate. We calculate EDPD spectra from the Co ($2p$) core level using a multiple scattering photoemission slab method[12] in which the $p\rightarrow d$ and $p\rightarrow s$ transition matrix elements[11,12] are explicitly evaluated at each photon energy. The incident photon is p polarized, and the electron exit direction is in the plane of photon incidence. For each EDPD spectrum, the polar angle between the photon incident direction and electron exit direction is kept fixed at 70°. The crystal is rotated in θ and ϕ to generate EDPD spectra at different outgoing electron directions. For the final-state multiple scattering, we use the exact Green's function structural propagator given in Eq. (13) to evaluate the near-field wave function.[12] In other words, while the separable form of

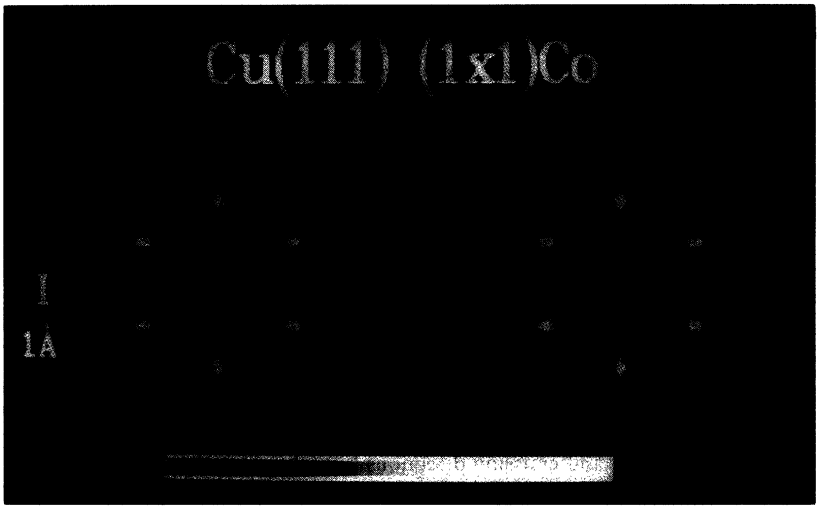

FIG. 3. The images of 18 Co atoms viewed in a plane passing through their atomic centers. The cross in each panel marks the position of the emitter.

the Green's function shown in Eq. (14) is used to simplify the discussion in Sec. III, the exact Green's function is used to generate the EDPD spectra that are used in the image reconstruction. Also, because we use the actual energy-dependent photoemission excitation matrix elements and scattering t matrices, the coefficients $A(\mathbf{k})$ and $B(\mathbf{k})$ in Eq. (18) contain the phase shift effects.[9]

The EDPD spectra from the Co ($2p$) core level are calculated in the 100 eV to 400 eV kinetic energy range. A uniform energy grid of $\Delta k = 0.28$ Å^{-1} is used. Since $\Delta E = k\Delta k$, it corresponds to using $\Delta E = 11$ eV at 100 eV and $\Delta E = 22$ eV at 400 eV. The EDPD spectra are normalized according to the prescription given after Eq. (1). To image the near-neighbor atoms in the surface layer, we normally need only a few EDPD spectra. However, in the example given here, we include a complete mesh of (θ,ϕ) angles to cover the entire 2π solid angle so that these results are directly comparable to those of electron-emission holography (EEH).[6,7] We shall return to this point in Sec. VI. Since the system has C_{3v} symmetry, we need a (θ,ϕ) mesh to cover the $\theta = 0°$ to 90° and $\phi = 0°$ to 30° hemispheric sections. The images are reconstructed according to Eqs. (2) and (6), and the form $u_1(\mathbf{R}) = |\phi(\mathbf{R})|$ is used.

Figure 3, left panel, shows the images when viewed in a plane passing through the Co atomic nuclei. The cross at the center of the left panel marks the position of the emitting atom. The six nearest-neighbor atoms and another shell of six next-nearest-neighbor atoms are sharply imaged. The full widths at half magnitude (FWHM) of these images are well below 1 Å. The third-shell six neighbors are shadowed by the first-shell atoms. The images of these shadowed atoms are split as triplets—an example of the artifacts caused by multiple scattering events.[16] Apart from these artifacts, the noise level in the entire space of the images is extremely low, indicating that all other multiple scattering paths are effectively eliminated. In particular, the high-intensity noise near the origin so common in single-energy electron-emission holography[17,18] is absent here.

In the right panel of Fig. 3, the same images are shown with circles surrounding each image. The center of each circle marks the correct atomic position. We note that the images of the first two shells are phase shifted by ~0.1 to 0.3 Å from the correct atomic positions.[9] For the shell of third nearest neighbors, the largest spot falls inside the circle while the two multiple scattering artifacts are weaker and substantially shifted from the atomic position. Finally, the lack of complete sixfold symmetry in the reconstructed image is due to a C_{4v} network of points in the xy plane used in the Fourier transformation.

In the second example, we show that as few as four to ten EDPD spectra can be used to image the nearest- and next-nearest-neighbor atoms in the surface Ni layer of the Ni(001) $c(2\times2)$-S system. To demonstrate this, we first calculated EDPD spectra from the S($1s$) core level using the multiple scattering photoemission slab method mentioned earlier. The normalized EDPD spectra are calculated in the 100–450-eV kinetic energy range. The S atom is placed at a fourfold hollow site 1.3 Å above the Ni substrate.[19] In Fig. 4 we show this atomic arrangement in a schematic diagram. To illustrate the flexibility of this approach, we use a single $\theta = 50°$ and a range of ϕ angles taken on either side of the [010] mirror plane. The panels of Fig. 5 (from left to right, top to bottom) corre-

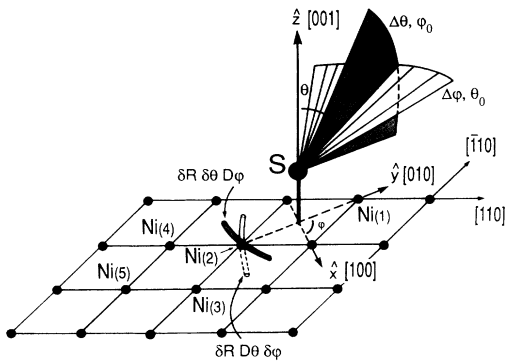

FIG. 4. Images $\delta R D\theta\delta\phi$ and $\delta R\delta\theta D\phi$ formed from EDPD spectra along $(\Delta\phi,\theta_0)$ and $(\Delta\theta,\phi_0)$ directions, respectively. The intersections of the images fix the atomic coordinates.

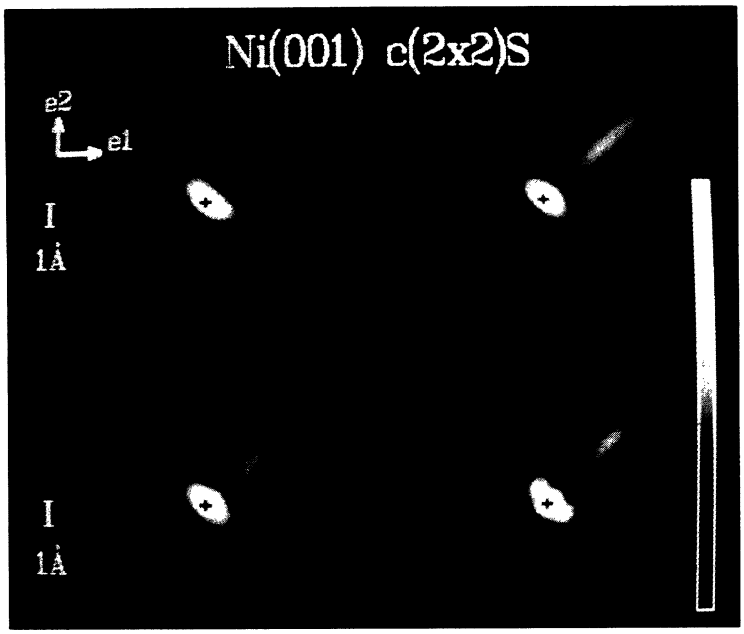

FIG. 5. Images of atoms Ni(2), (3), (4), and (5) in an xy plane 1.3 Å below the S atom for different $\Delta\phi$ ranges; $e1$ and $e2$ are along the [110] and [$\bar{1}$10] directions, respectively. The crystal orientation and atomic arrangements refer to those shown in Fig. 4.

spond, respectively, to images formed by using ϕ ranges of $\pm 15°$, $\pm 25°$, $\pm 35°$, and $\pm 45°$ on either side of [010] with an equal mesh of 5°. The images are viewed in an xy plane 1.3 Å below the S atom. Referring to Fig. 5, the large, thin cross at the center of each panel corresponds to the position of the S atom projected onto the xy plane. With a small $\Delta\phi$ range, e.g., $\pm 15°$ and $\pm 25°$, only very bright Ni(2) (small cross) and Ni(5) (thick cross), which is directly behind it, are resolved. As $\Delta\phi$ increases, e.g., $\geq \pm 35°$, the four Ni atoms in the back-scattering quadrant of Fig. 4, i.e., Ni(2), (3), (4), and (5), are separately resolved (the correct atomic positions are marked by small crosses). These results are independent of the choice of θ as long as we choose θ to enhance the S-Ni back-scattering geometry. Because [010] is along a mirror plane of the system, we have used respectively four, six, eight, and ten independent EDPD spectra to construct the images shown in the four panels of Fig. 5 (left to right, top to bottom).

While the purpose of Fig. 5 is to image the Ni atoms in the back-scattering quadrant, the diffraction fringes due to small-angle forward scattering are also present. These show up as elongated (flamelike) images in each panel. For example, the strongest elongated band is due to Ni(1), along the [010] direction—although the image position is substantially phase shifted by the strong forward-scattering factor.[9] In the bottom two panels, other elongated, flamelike atom images along with multiple scattering artifacts can be detected. The atom images correspond to the other Ni atoms in the forward-scattering half-plane (i.e., $y \geq 0$) of Fig. 4. Figure 5 demonstrates that substantially better-resolved images can be obtained using the back-scattering geometry than using the forward-scattering geometry. Because the wave number integral in Eq. (2) produces atom images with very poor resolution in the forward-scattering geometry, a two-step process was proposed:[7,8] phase-shift correction[9] is applied to determine the emitter-scatterer bond distance R_0 (usually to within ± 0.3 Å); the value of R_0 is used in a phase sum to form the atom image at $\mathbf{R}_0$.[7,8]

The configuration of the Ni images in the back-scattering quadrant (i.e., $y \leq 0$) in Fig. 5 and their distances from the S atoms establish its adsorption site. To determine the S—Ni(2) bond length, we sum over Fourier transformed functions of EDPD spectra (also in the 100–450-eV range) calculated at ϕ_0 = [010] and a set of θ values 15°–75° in equal steps of 5°. Figure 6 shows the image along the zy plane which passes through the S emitter. The cross in the center marks the S position, and the thick cross marks the Ni(2) atomic position. The error in the image position is less than 0.3 Å.

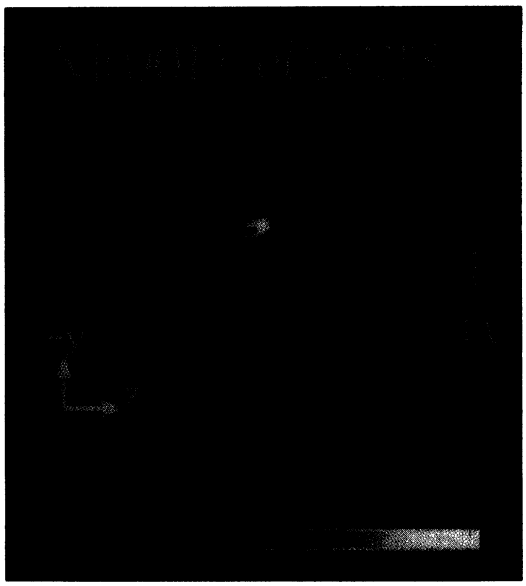

FIG. 6. Image of the Ni(2) atom in a yz plane passing through the S emitter. The coordinate system is according to Fig. 4.

V. WHY DOES DATA INVERSION WORK FOR SRI-EDPD? A COMPARISON WITH EXAFS

EXAFS is a direct method with a high-precision determination of near-neighbor bond distances from an emitter. In EXAFS, the data base is $\chi(k)$ where the absorption cross section internally integrates the diffraction pattern over 4π solid angles at each energy, i.e.,

$$\chi(k)=\int \chi(k,\theta,\phi)d\Omega \ . \tag{24}$$

It is well established that multiple scattering effects are eliminated in EXAFS, except for outer shell atoms that are directly shadowed by the inner shell atom.[20] Because EXAFS integrates $\chi(k,\theta,\phi)$ over angular space, what is left is a one-dimensional quantity $\chi(k)$. The direct information obtained from inversion of $\chi(k)$ is the scalar bond length R_j.

SRI-EDPD uses a similarly sized data base as EXAFS, but here, angle-resolved information $\chi(E$ or $k,\theta,\phi)$ is retained. The inversion of three-dimensional data $\chi(k,\theta,\phi)$ to real space via Eqs. (2) and (6) yields three-dimensional vector information (R_{jx},R_{jy},R_{jz}). Artifacts due to multiple scattering events are spatially dispersed and eliminated. Therefore, the reasons why SRI-EDPD works are exactly the same as those for EXAFS, except the former provides 3D vector information, while the latter provides scalar information of atomic positions.

VI. COMPARISON WITH ELECTRON-EMISSION HOLOGRAPHY

Photoelectron diffraction (PED) is a well-understood process.[21] Measurements initially focused on the angular anistrophy at fixed energy.[22–26] We have, for some time, emphasized the advantages of analyzing EDPD spectra.[27–29] EDPD spectra were measured at normal emission and off-normal emission directions by Shirley and others.[30–36] Recently, analysis of EDPD spectra were extended to the study of clean surfaces,[37] by measuring photoelectrons emitted from surface-shifted core levels.

More recently, Szoke recast photoelectron diffraction in a description analogous to electron holography.[38] Barton[17] proposed that the Helmholtz-Kirchoff integral

$$\phi(\mathbf{R})=\left|\int \chi(k_0\hat{\mathbf{k}})e^{i\hat{\mathbf{k}}\cdot\mathbf{R}}d\Omega_{\hat{\mathbf{k}}}\right| \tag{25}$$

would produce high-intensity spots at atomic positions $\mathbf{R}_j$. This hypothesis has led to a number of studies based on simulated and measured diffraction data.[6–10,17,18,39–43] Our studies based on calculated spectra[7–10,41] as well as measured data[43] showed that the integral given in Eq. (25), derived from an analogy with optical holography, does not work for PED because photoelectrons scatter too strongly inside a material. We can understand the reasons by examining the coefficients given in Eq. (18). For a weak-scattering particle, the multiple scattering terms are small, i.e., $|B(\mathbf{k})|\approx 0$ and the $\hat{\mathbf{k}}$ *dependence* of the single-scattering coefficient is weak, i.e., $A(\mathbf{k})\approx Ae^{i\phi}$. Then the integral of Eq. (25) does satisfy the stationary-phase condition and $\phi(\mathbf{R})$ peaks at $\mathbf{R}=\mathbf{R}_\beta$ with a magnitude proportional to $|A|$.

However, for photoelectrons, the electron-atom scattering is strong. With the strong scattering, even the single-scattering term $A(\mathbf{k})=f(\hat{\mathbf{k}}\cdot\hat{\mathbf{R}}_\beta)F_D(\hat{\mathbf{R}}_\beta)F_D^{-1}(\hat{\mathbf{k}})$ causes a shift in the image position due to its $\hat{\mathbf{k}}$ dependence.[9] But far more serious is the fact that the multiple scattering coefficient from Eq. (18)

$$M(\mathbf{k})=A(\mathbf{k})\frac{e^{ik\mathbf{R}_\beta}}{R_\beta}+B(\mathbf{k})\frac{e^{ikR_\gamma}}{R_\gamma}\frac{e^{ik|\mathbf{R}_\beta-\mathbf{R}_\gamma|}}{|\mathbf{R}_\beta-\mathbf{R}_\gamma|}+\cdots \tag{26}$$

is dependent on the local structure $|\mathbf{R}_\beta-\mathbf{R}_\gamma|$ of the system. In unknown systems, there is no *a priori* way to estimate either the magnitude or the phase of $M(\mathbf{k})$ as long as $A(\mathbf{k})$ and $B(\mathbf{k})$ are comparable in magnitude. Therefore, the holographic transformation given by Eq. (25) generally fails.[7–10,40,43]

VII. CONCLUSIONS

We have presented the method of SRI-EDPD and demonstrated how three-dimensional atom images are obtained by inverting energy-dependent photoelectron-diffraction spectra. The method is rooted in photoelectron diffraction (PED) and is an extension of ARPEFS to vector space. Starting from the three-dimensional data base $\chi(E,\theta,\phi)$, vector position information (R_x,R_y,R_z) are obtained for atoms within the mean-free path of the outgoing photoelectron.

In the measurement of photoelectron diffraction, it is important to determine accurately the emission peak and the background electrons at each point of (E, θ, and ϕ). This is a rather time-consuming process. The method of SRI-EDPD is practical because it requires considerably less data base than conventional summed-energy EEH.[6,7] By using the intersection of images with $\delta\mathbf{R}\delta\phi D\theta$ and $\delta RD\phi\delta\theta$ characteristics, the required data base scales as $(N_\theta+N_\phi)$. Another difference is that in SRI-EDPD, the quantities $I_D(k\hat{\mathbf{k}})$ and A used to normalize $\chi(k\hat{\mathbf{k}})$ in Eq. (2) are *energy smoothed* and energy averaged for each EDPD spectrum. In summed-energy electron-emission holography,[6,7] the smoothing and averaging are done over angles at each energy. The two processes are not equivalent. Finally, by emphasizing the small take-off polar angles from the surface and using the photon's $\mathbf{A}$ vector to enhance the image intensity in particular directions, SRI-EDPD is effective for viewing the first couple of layers of a surface or interface. In many instances, e.g., in bulk-emission systems, inclusion of a large angular range is actually undesirable. On GaAs(001)-2×4, for example, surface dimers cannot be seen by conventional EEH using data covering a large angular cone because the signal from bulk layers overwhelms those coming from the surface.[43] However, with SRI-EDPD, it is possible to use a spread of ϕ angles at glancing polar angles to image the As dimers on the surface. These results will be presented elsewhere.[44]

ACKNOWLEDGMENTS

This work was supported in part by NSF Grants Nos. DMR-8805938 and INT-9011271.

[1]Z. Hussain, D. A. Shirley, C. H. Li, and S. Y. Tong, Proc. Natl. Acad. Sci. U.S.A. **78**, 5293 (1981).
[2]P. J. Orders and C. S. Fadley, Phys. Rev. **27**, 781 (1983).
[3]J. J. Barton, C. C. Bahr, Z. Hussain, S. W. Robey, J. G. Tobin, L. E. Klebanoff, and D. A. Shirley, Phys. Rev. Lett. **51**, 272 (1983).
[4]J. J. Barton, C. C. Bahr, S. W. Robey, Z. Hussain, E. Umbach, and D. A. Shirley, Phys. Rev. B **34**, 3807 (1986).
[5]L. Q. Wang, A. E. Schach von Wittenau, Z. G. Ji, L. S. Wang, Z. Q. Huang, and D. A. Shirley, Phys. Rev. B **44**, 1292 (1991).
[6]J. J. Barton and L. J. Terminello, in *The Structure of Surfaces—III,* edited by S. Y. Tong, M. A. Van Hove, X. Xie, and K. Takayanagi (Springer, Berlin, 1991); J. J. Barton, Phys. Rev. Lett. **67**, 3106 (1991).
[7]S. Y. Tong, Hua Li, and H. Huang, Phys. Rev. Lett. **67**, 3102 (1991).
[8]S. Y. Tong, H. Huang, and Hua Li, in *Advances in Surface and Thin Film Diffraction,* edited by T. C. Huang, P. I. Cohen, and D. J. Eaglesham, MRS Symposia Proceedings No. 208 (Materials Research Society, Pittsburgh, 1991), p. 13; H. Huang, Hua Li, and S. Y. Tong, Phys. Rev. B **44**, 3240 (1991).
[9]S. Y. Tong, C. M. Wei, T. C. Zhao, H. Huang, and Hua Li, Phys. Rev. Lett. **66**, 60 (1991).
[10]C. M. Wei, T. C. Zhao, and S. Y. Tong, Phys. Rev. B **43**, 6354 (1991); H. C. Poon, D. Snider, and S. Y. Tong, *ibid.* **33**, 2198 (1986).
[11]See, for example, S. Y. Tong and C. H. Li, in *Critical Reviews in Solid State and Materials Sciences,* edited by D. E. Schuele and R. W. Hoffman (CRC, Cleveland, OH, 1981), Vol. 10, p. 209.
[12]C. H. Li, A. R. Lubinsky, and S. Y. Tong, Phys. Rev. B **17**, 3128 (1978).
[13]S. Y. Tong, H. C. Poon, and D. R. Snider, Phys. Rev. B **32**, 2096 (1985).
[14]J. J. Rehr and R. C. Albers, Phys. Rev. B **41**, 8139 (1990).
[15]For a detailed discussion of the "mixed" multiple scattering events, see S. Y. Tong and Hua Li (unpublished).
[16]For the derivation of the factor 1.2Γ, see S. Y. Tong, Hua Li, and H. Huang, Phys. Rev. B (to be published).
[17]J. J. Barton, Phys. Rev. Lett. **61**, 1356 (1988).
[18]G. R. Harp, D. K. Saldin, and B. P. Tonner, Phys. Rev. Lett. **65**, 1012 (1990).
[19]J. E. Demuth, D. W. Jepsen, and P. M. Marcus, Phys. Rev. Lett. **31**, 540 (1973).
[20]P. A. Lee and J. B. Pendry, Phys. Rev. B **11**, 2795 (1975).
[21]A. Liebsch, Phys. Rev. Lett. **32**, 1203 (1974).
[22]D. P. Woodruff, Surf. Sci. **53**, 538 (1975).
[23]N. V. Smith, P. K. Larsen, and S. Chiang, Phys. Rev. B **16**, 2699 (1977).
[24]S. Kono, C. S. Fadley, N. F. T. Hall, and Z. Hussain, Phys. Rev. Lett. **41**, 117 (1978).
[25]D. P. Woodruff, D. Norman, B. W. Holland, N. V. Smith, H. H. Farrell, and M. M. Traum, Phys. Rev. Lett. **41**, 1130 (1978).
[26]R. L. Benbow, M. R. Thuler, Z. Hurych, K. H. Lau, and S. Y. Tong, Phys. Rev. B **28**, 4160 (1983).
[27]S. Y. Tong, C. H. Li, and A. R. Lubinsky, Phys. Rev. Lett. **39**, 498 (1977).
[28]C. H. Li and S. Y. Tong, Phys. Rev. Lett. **40**, 46 (1978).
[29]S. Y. Tong and C. H. Li, Bull. Am. Phys. Soc. **23**, 417 (1978); C. H. Li and S. Y. Tong, Phys. Rev. B **19**, 1769 (1979); Phys. Rev. Lett. **42**, 901 (1979); **43**, 526 (1979).
[30]S. D. Kevan, D. H. Rosenblatt, D. Denley, B. C. Lu, and D. A. Shirley, Phys. Rev. Lett. **41**, 1565 (1978).
[31]D. H. Rosenblatt, J. G. Tobin, M. G. Mason, R. F. David, S. D. Kevan, D. A. Shirley, C. H. Li, and S. Y. Tong, Phys. Rev. B **23**, 3828 (1981); S. D. Kevan, R. F. Davis, J. G. Tobin, D. A. Shirley, C. H. Li, and S. Y. Tong, Phys. Rev. Lett. **46**, 1629 (1981).
[32]D. H. Rosenblatt, S. D. Kevan, J. G. Tobin, D. A. Shirley, Y. Huang, and S. Y. Tong, Phys. Rev. B **26**, 1812 (1982).
[33]J. G. Tobin, L. E. Klebanoff, D. H. Rosenblatt, R. F. Davis, E. Umbach, A. G. Baca, D. A. Shirley, Y. Huang, W. M. Kang, and S. Y. Tong, Phys. Rev. B **26**, 7076 (1982).
[34]S. Y. Tong, W. M. Kang, D. H. Rosenblatt, J. G. Tobin, and D. A. Shirley, Phys. Rev. B **27**, 4632 (1983).
[35]D. H. Rosenblatt, S. D. Kevan, J. G. Tobin, D. A. Shirley, J. C. Tang, and S. Y. Tong, Phys. Rev. B **26**, 3181 (1982).
[36]J. G. Tobin, M. K. Wagner, X. Q. Guo, and S. Y. Tong, in *Advances in Surface and Thin Film Diffraction* (Ref. 8), p. 283.
[37]R. A. Bartynski, D. Heskett, K. Garrison, G. Watson, D. M. Zehner, W. N. Mei, S. Y. Tong, and X. Pan, Phys. Rev. B **40**, 5340 (1989).
[38]A. Szoeke, in *Proceedings of the Topical Meeting on Short Wavelength Coherent Radiation,* edited by D. T. Attwood and J. Boker, AIP Conf. Proc. No. 147 (AIP, New York, 1986).
[39]S. Thevuthasan, G. S. Herman, A. P. Kaduwela, R. S. Saiki, Y. J. Kim, and C. S. Fadley, Phys. Rev. Lett. **67**, 469 (1991).
[40]A. Stuck, D. Naumovic, H. A. Aebischer, T. Greber, J. Osterwalder, and L. Schlapbach, Surf. Sci. **264**, 380 (1992).
[41]C. M. Wei, T. C. Zhao, and S. Y. Tong, Phys. Rev. Lett. **65**, 2278 (1990).
[42]S. Hardcastle, Z. L. Han, G. R. Harp, J. Zhang, B. L. Chen, D. K. Saldin, and B. P. Tonner, Surf. Sci. Lett. **245**, L190 (1991).
[43]S. A. Chambers, V. A. Loebs, Hua Li, and S. Y. Tong, J. Vac. Sci. Technol. B (to be published).
[44]Hua Li and S. Y. Tong (unpublished).

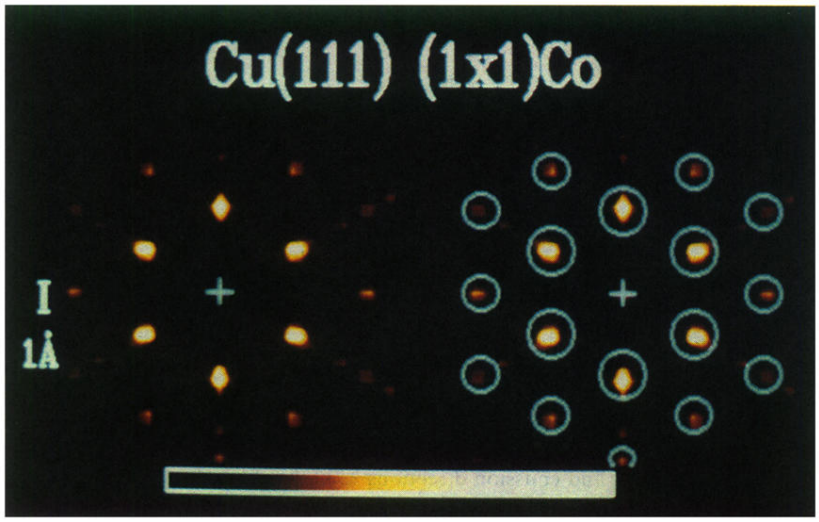

FIG. 3. The images of 18 Co atoms viewed in a plane passing through their atomic centers. The cross in each panel marks the position of the emitter.

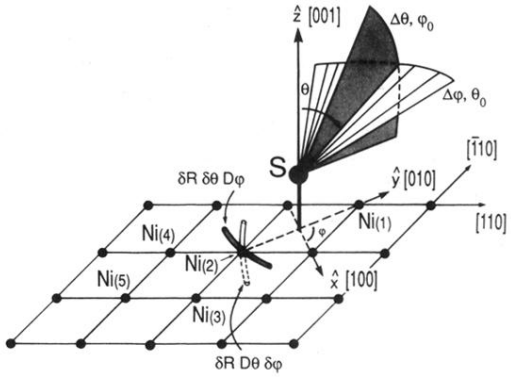

FIG. 4. Images $\delta R D\theta\delta\phi$ and $\delta R\delta\theta D\phi$ formed from EDPD spectra along $(\Delta\phi,\theta_0)$ and $(\Delta\theta,\phi_0)$ directions, respectively. The intersections of the images fix the atomic coordinates.

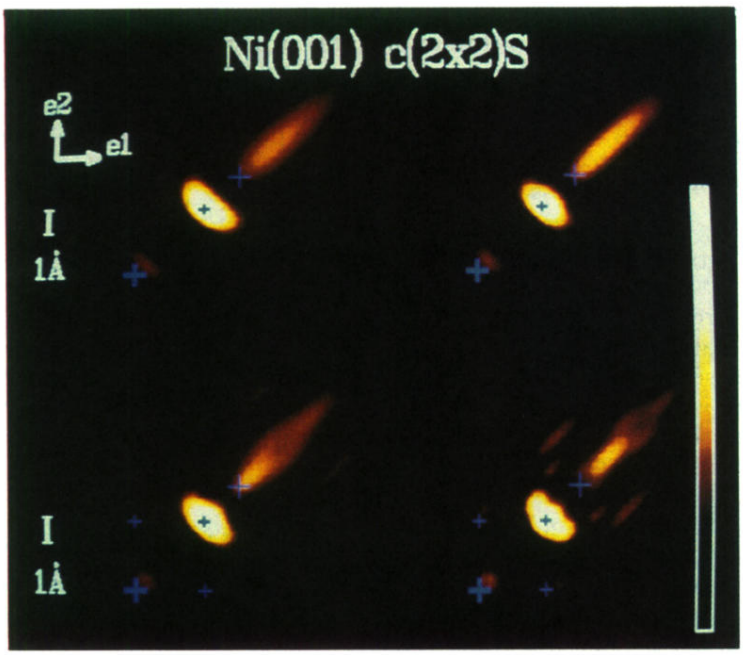

FIG. 5. Images of atoms Ni(2), (3), (4), and (5) in an xy plane 1.3 Å below the S atom for different $\Delta\phi$ ranges; $e1$ and $e2$ are along the [110] and [$\bar{1}$10] directions, respectively. The crystal orientation and atomic arrangements refer to those shown in Fig. 4.

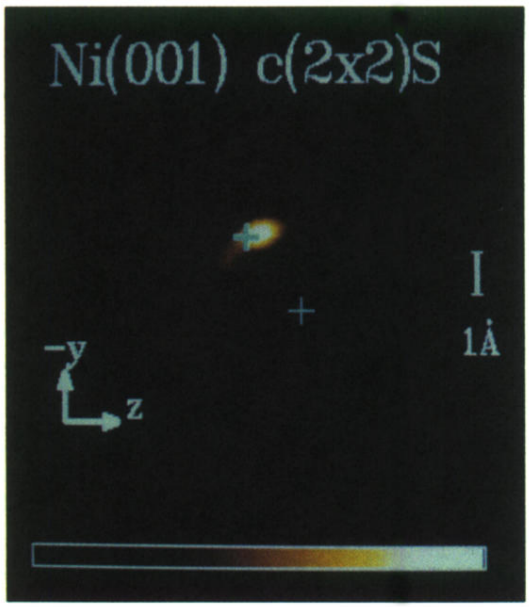

FIG. 6. Image of the Ni(2) atom in a *yz* plane passing through the S emitter. The coordinate system is according to Fig. 4.